A Tomographic Formulation of Spotlight-Mode Synthetic Aperture Radar

DAVID C. MUNSON, JR., MEMBER, IEEE, JAMES DENNIS O'BRIEN, STUDENT MEMBER, IEEE,

AND W. KENNETH JENKINS, SENIOR MEMBER, IEEE

Abstract—Spotlight-mode synthetic aperture radar (spotlight-mode SAR) synthesizes high-resolution terrain maps using data gathered from multiple observation angles. This paper shows that spotlight-mode SAR can be interpreted as a tomographic reconstruction problem and analyzed using the projection-slice theorem from computer-aided tomography (CAT). The signal recorded at each SAR transmission point is modeled as a portion of the Fourier transform of a central projection of the imaged ground area. Reconstruction of a SAR image may then be accomplished using algorithms from CAT. This model permits a simple understanding of SAR imaging, not based on Doppler shifts. Resolution, sampling rates, waveform curvature, the Doppler effect, and other issues are also discussed within the context of this interpretation of SAR.

I. INTRODUCTION

BOTH computer-aided tomography (CAT) and synthetic aperture radar (SAR) are well-known techniques for constructing high-resolution images by processing data obtained from many different perspective views of a target area. The CAT scan, as it is familiarly termed now, is an X-ray technique which enables the imaging of two-dimensional cross sections of solid objects [1], [2]. In particular, tomography is used extensively for noninvasive medical examination of internal organs and in nondestructive testing of manufactured items. Although SAR is well known to a more exclusive community, it too is a well-developed technique for producing high-resolution images. In a SAR system, the desired image is a terrain map. The data are collected by means of an airborne or spaceborne microwave radar which illuminates the target area from different perspectives.

An early form of SAR, known as unfocused strip mapping, was demonstrated experimentally at the University of Illinois as far back as the early 1950's [3]. In strip-mapping SAR (both focused and unfocused), the position of the antenna remains fixed relative to the aircraft, thereby illuminating a strip of terrain as the aircraft flies. Proper processing of the returned signals allows the effective synthesis of a very large antenna, providing high resolution [3]-[6]. Extensive developmental work on optical processing of data collected in strip-mapping SAR was subsequently carried out by Brown and coworkers at what is now the Environmental Research Institute of Michigan. Walker [7], working with Brown, made a breakthrough in characterizing the requirements for optically processing coherent radar data collected from targets placed on a rotating platform, an experimental setup designed to simulate an airborne radar flying around a stationary ground patch—this was, in essence, the first spotlight-mode SAR. In this

paper, we will focus on this latter type of SAR, in which the physical antenna is steered so that the same terrain area remains illuminated during a long data-collection interval [5], [7]-[9]. Spotlight-mode SAR is able to provide higher resolution of a more limited area than strip-mapping SAR, because the same terrain area is observed from many different angles.

The fact that CAT and spotlight-mode SAR have developed independently—CAT having attracted the interest of biomedical researchers, and SAR that of communications and radar specialists—has obscured a remarkable similarity of principle which they share. CAT processing has generally been characterized by the projection-slice theorem [1], [2], [10], [11], while spotlight-mode SAR processing has been described in the radar language of Doppler filtering [7], [8], [12]. A survey of published literature on SAR may not lead one to suspect that SAR is a distant cousin of CAT. The major objective of this paper is to demonstrate that CAT and SAR are, in fact, very similar concepts. It will be shown that spotlight-mode SAR can be interpreted as a tomographic reconstruction problem, and that the signal processing theory can be characterized in terms of the projection-slice theorem. The advantages in developing this connection are several. First, research into mathematical methods and algorithms developed in one field may be transferred to the other. Second, the tomographic interpretation simplifies the understanding of SAR, especially for those not versed in radar terminology. A third advantage is that the role of coherence is underscored and the speckle phenomenon is easily explained when SAR is interpreted as a narrow-band version of CAT.

Some of these concepts have been examined in relation to acoustic imaging using sources emitting short pulses or polychromatic continuous-wave (CW) illumination over circular apertures [13], [14]. Several authors have also discussed SAR utilizing polychromatic CW illumination over circular apertures (see, for instance, [15]). In practice, though, airborne radars are not coherent over extended flight trajectories due to unavoidable phase errors (caused by atmospheric granularity and motion error) and due to the angular dependence of the reflectors being imaged. Chen and Andrews [16] discuss the spotlight-mode SAR problem for sources emitting sinusoidal waveforms. Herman [2], [17] discusses related work in other fields, including radio astronomy.[1]

To introduce our basic approach, Section II reviews the projection-slice theorem and summarizes the fundamental principles of tomographic reconstruction. The mathematical formulation of SAR in Section III contains the significant contribution of this paper. If linear FM waveforms are transmitted during spotlight-mode operation, it is demonstrated that the demodulated wave-

[1]Mensa *et al.* [18] also present some closely related work on microwave tomographic imaging. Reference [18] was published while this paper was still in review.
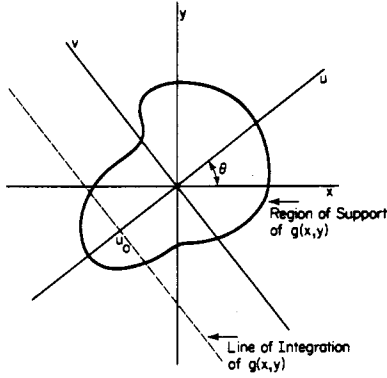
Fig. 1.   Line of integration for determining the projection $p_\theta(u_0)$.

form obtained at each look angle approximates a piece of the one-dimensional (1-D) Fourier transform of a central projection of the ground patch at a corresponding projection angle. A similar statement has been made by Brown [19] in his interpretation and generalization of the work by Walker [7]. Together with the projection-slice theorem, this enables SAR and the processing of SAR data to be viewed in terms similar to CAT, although the physical constraints and data-gathering limitations are somewhat different. SAR is then discussed as a narrow-band version of CAT and the possibility of using CAT processing algorithms, such as convolution backprojection, for SAR is presented. Finally, for completeness, Section IV addresses the issues of resolution, sampling rates, wavefront curvature, quadratic phase errors, effect of Doppler and time-varying range, and the modification of results for slant-plane geometry.

II.   BRIEF REVIEW OF COMPUTER-AIDED TOMOGRAPHY

Computer-aided tomography is a technique for providing a two-dimensional (2-D) cross-sectional view of a three-dimensional (3-D) object through digital processing of many 1-D projectional views taken from different look angles. These projectional views are obtained by passing sets of narrow X-ray beams through the object and detecting their intensities using an array of sensors. If desired, a 3-D reconstruction may be obtained by this technique as a collection of parallel cross sections.

A.   Projection-Slice Theorem

The principle underlying the theory of CAT is the projection-slice theorem [1], [2], [10], [11]. Let $g(x, y)$ be an unknown signal that is to be reconstructed from its projections. The Fourier transform of g is defined as

$$G(X, Y) = \int_{-\infty}^{\infty} \int_{-\infty}^{\infty} g(x, y) e^{-j(xX + yY)} \, dx \, dy$$

so that

$$g(x, y) = \frac{1}{4\Pi^2} \int_{-\infty}^{\infty} \int_{-\infty}^{\infty} G(X, Y) e^{j(xX + yY)} \, dX \, dY. \quad (1)$$

The projection of g at angle θ is formally given by

$$p_\theta(u) = \int_{-\infty}^{\infty} g(u \cos \theta - v \sin \theta, u \sin \theta + v \cos \theta) \, dv \quad (2)$$

where $p_\theta(u)$ evaluated at $u = u_0$ is simply a line integral in the direction of the v axis as illustrated in Fig. 1. Note that the u axis forms an angle θ with the x axis. The function $p_\theta(u)$ represents a series of such line integrals for each value of θ.
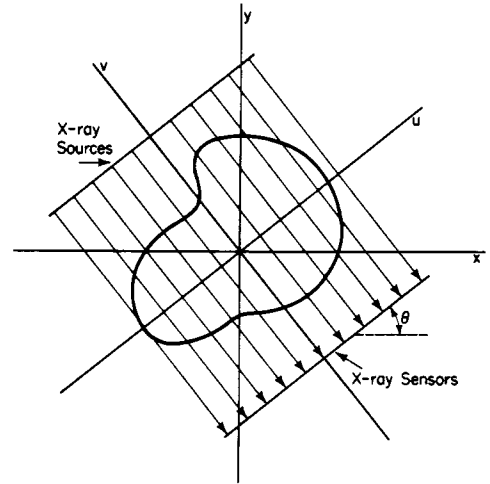
The 1-D Fourier transform of $p_\theta(u)$ is given by

Fig. 2.   A parallel-beam X-ray tomography system.

$$P_\theta(U) = \int_{-\infty}^{\infty} p_\theta(u) e^{-juU} \, du.$$

Using this notation, the statement of the projection-slice theorem is simply

$$P_\theta(U) = G(U \cos \theta, U \sin \theta) \quad (3)$$

that is, the Fourier transform of the projection at angle θ is a "slice" of the 2-D transform $G(X, Y)$ taken at an angle θ with respect to the X axis.

B.   Tomographic Reconstruction

In X-ray tomography, $g(x, y)$ is an unknown cross-sectional attenuation coefficient which is to be measured. Samples of the projection $p_\theta(u)$ are obtained in a parallel-beam system with an array of X-ray sources and detectors oriented at an angle θ with respect to the x axis, as shown in Fig. 2. Since the intensity of a received X-ray beam exhibits exponential dependence on the line integral of g [2], projections of g are found in terms of the logarithms of the measured intensities, i.e.,

$$p_\theta(u) = -\log \frac{I_\theta(u)}{I_0}$$

where I_0 is the intensity of the X-ray source and $I_\theta(u)$ is the received intensity at the detector. Projections $p_{\theta_i}(u)$ are obtained at equally spaced angles $\theta = \theta_i$ by rotating either the object or the array of X-ray sources and detectors through a set of discrete angles spanning 360°.

In present tomographic systems, it is common to reconstruct the attenuation coefficient $g(x, y)$ from the projections $p_{\theta_i}(u)$ via the convolution backprojection method [1]. This method will be described later in conjunction with a modification for SAR. An alternate method is direct Fourier domain reconstruction. It is the direct Fourier technique which is used primarily in SAR and it has also been considered for use in tomography [11], [20]. Using the direct Fourier technique, $g(x, y)$ is reconstructed from samples $p_{\theta_i}(u_j)$ of its projections as follows. For each angle θ_i, uniformly spaced samples of the Fourier transform $P_{\theta_i}(U)$ are computed from $\{ p_{\theta_i}(u_j) \}_{j=1}^{N}$ via the fast Fourier transform (FFT). From the projection-slice theorem, (3), the samples of $P_{\theta_i}(U)$ are samples of $G(X, Y)$ along a line at angle θ_i with the X axis. Thus the series of 1-D FFT's for the various θ_i provides samples of $G(X, Y)$ on the polar grid shown in Fig. 3. Interpolating the polar samples of G to a Cartesian grid allows the efficiencies of the 2-D inverse FFT to be utilized to approximate g on a
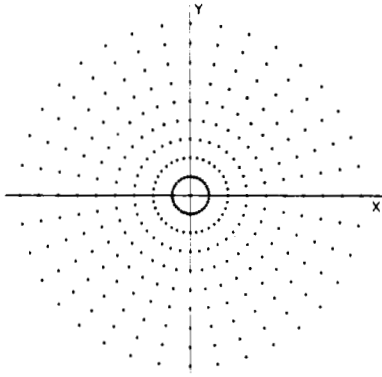
Fig. 3. Locus of known samples of $G(X, Y)$ (Fourier domain).

Cartesian grid [9], [11], [20]. It must be said, though, that no really "fast" algorithm has yet been devised to compute g from the polar samples of G (although this is an area of research [2], [11], [17], [20]–[23]); unless a time-consuming interpolation is carried out prior to employing the FFT, the image quality produced by the Fourier technique will be noticeably worse than that provided by the convolution backprojection method.

III. SPOTLIGHT-MODE SYNTHETIC APERTURE RADAR

A. Introduction

The limiting factor in the azimuthal (cross-range) resolving capabilities of an ordinary ranging radar is the antenna beamwidth in the distant field. For airborne operation, a narrow beamwidth requires an impractically large antenna. Spotlight-mode SAR effectively avoids this requirement by collecting radar returns from many different angular views of a target. By properly processing the return signals, very high resolution in azimuth can be achieved. High resolution in range may be achieved by transmitting high-bandwidth pulses as in a conventional radar.

The geometry for data collection in a spotlight-mode SAR is shown in Fig. 4. The x–y coordinate system (denoting *range* and *azimuth* coordinates, respectively) is centered on a relatively small patch of ground illuminated by a narrow RF beam from the moving radar. As the radar traverses the flight path, the radar beam, as operating in the spotlight mode, is continuously pointed in the direction (angle θ) of the ground patch. At points corresponding to equal increments of θ, high-bandwidth pulses (such as linear FM) are transmitted to the ground patch and echoes are then received and processed. The radar return yields a projectional view of the target, provided the phase front of the radio waves exhibits no significant curvature. This view turns out, in fact, to be a band-pass filtered projection of the ground-patch reflectivity, since the radio waves are narrow-band.

As the aircraft moves with respect to the target patch, the received signal undergoes a slight Doppler shift (to be discussed later) which varies according to the observation angle. The SAR imaging equations can be derived as a function of either the Doppler shift or the underlying change in viewing angle. It is important to emphasize, however, that the imaging principle employed in spotlight-mode SAR is tomographic, rather than Doppler based. That is, although the radar antenna must be moved from point to point to obtain different viewing angles, successful imaging is not dependent on a difference in relative velocity between the antenna and ground patch during pulse transmission and reception. As far as the imaging mechanism is
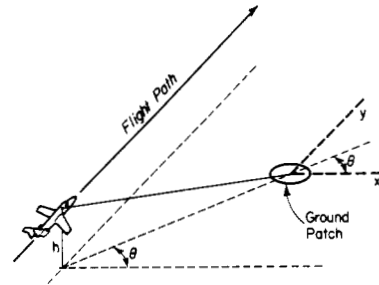

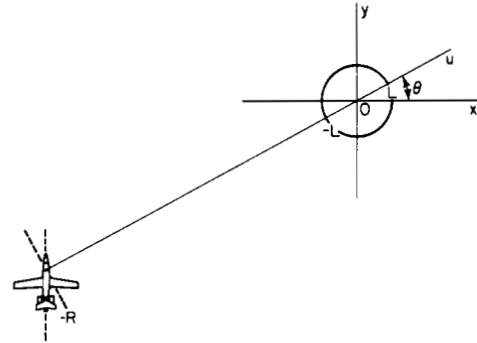Fig. 4. Geometry for data collection in spotlight-mode SAR.

Fig. 5. Ground-plane geometry for data collection in spotlight-mode SAR.

concerned, the aircraft could completely stop at each transmission point in space and the SAR would still work properly.

B. Basic SAR Derivation

If it is assumed that the depression angle from the radar to the ground patch is zero, the geometry reduces to Fig. 5. Later, it will be indicated how the results can be modified for the case of a nonzero depression angle (i.e., the height $h \neq 0$). In Fig. 5, the reflectivity density of the ground patch is modeled by the complex function[2] $g(x, y)$ where a sinusoid reflected from a point (x_0, y_0) is scaled in amplitude by $|g(x_0, y_0)|$ and shifted in phase by $\angle g(x_0, y_0)$ where $g(x, y) = |g(x, y)| \exp(j \angle g(x, y))$. Furthermore, it is assumed that $g(x, y)$ is constant over the range of frequencies and range of viewing angles θ employed by the radar.

At angle θ, let the radar transmit a linear FM chirp pulse $\mathrm{Re}\{s(t)\}$, where

$$s(t) = \begin{cases} e^{j(\omega_0 t + \alpha t^2)}, & |t| \leq \dfrac{T}{2} \\ 0, & \text{otherwise} \end{cases} \quad (4)$$

ω_0 is the RF carrier frequency and 2α is the FM rate. The return signal from a differential area centered on the point (x_0, y_0) at a distance R_0 from the radar will be

$$r_0(t) = A|g(x_0, y_0)| \cos\left(\omega_0\left(t - \frac{2R_0}{c}\right) + \alpha\left(t - \frac{2R_0}{c}\right)^2 \right.$$
$$\left. + \angle g(x_0, y_0) \right) dx\, dy$$

---

[2] The amplitude scaling occurs because only a fraction of the incident radiation is reflected back to the radar. The phase shift of the reflected wave may be caused by several factors; foremost is probably the shift at the air/target interface due to the difference between the dielectric constants of air and the target material. This effect is similar to that observed at the boundary of two waveguides having different characteristic impedances where at least one of the waveguides is dissipative [24]. The phase shift is also due to the tendency of the RF radiation to creep around target surfaces and its ability to penetrate soft objects and be reflected from within.

where A accounts for propagation attenuation, c is the speed of light, and $2R_0/c$ accounts for the two-way travel time from radar to target. The return $r_0(t)$ is written more simply as

$$r_0(t) = A \cdot \mathrm{Re}\left\{ g(x_0, y_0) s\left(t - \frac{2R_0}{c} \right) \right\} dx \, dy. \qquad (5)$$

In Fig. 5, points in the ground patch equidistant from the radar lie on an arc, but for a typical system $R \gg L$, so that this arc is nearly a straight line. Therefore, taking $p_\theta(u)$ to be the line integral given by (2), it follows from (5), by superposition,[3] that the return signal from a differential line of scatterers normal to the u axis at $u = u_0$ is given by

$$r_1(t) = A \cdot \mathrm{Re}\left\{ p_\theta(u_0) s\left(t - \frac{2(R + u_0)}{c} \right) \right\} du.$$

If $R \gg L$, the attenuation A may be taken as a constant. Therefore, the return from the entire ground patch can be approximated by the integral of r_1 over u, given by

$$r_\theta(t) = A \cdot \mathrm{Re}\left\{ \int_{-L}^{L} p_\theta(u) s\left(t - \frac{2(R + u)}{c} \right) du \right\}. \qquad (6)$$

This expression has the form of a convolution, thus the transform of p_θ can be obtained by Fourier methods over a range of frequencies determined by the bandwidth of $s(\cdot)$. For our case though, $s(\cdot)$ is a chirp pulse, and a different form of processing is customarily used. Substituting (4) into (6) gives

$$r_\theta(t) = A \cdot \mathrm{Re}\left\{ \int_{-L}^{L} p_\theta(u) \exp\left\{ j\left[\omega_0\left(t - \frac{2(R + u)}{c} \right) \right.\right.\right.$$
$$\left.\left.\left. + \alpha\left(t - \frac{2(R + u)}{c} \right)^2 \right] \right\} du \right\} \qquad (7)$$

on the interval[4]

$$-\frac{T}{2} + \frac{2(R + L)}{c} \leqslant t \leqslant \frac{T}{2} + \frac{2(R - L)}{c}. \qquad (8)$$

Letting

$$\tau_0 = \frac{2R}{c}$$

be the round-trip delay to the center of the ground patch and mixing (multiplying) $r_\theta(t)$ with the reference chirp

$$\cos\left[\omega_0(t - \tau_0) + \alpha(t - \tau_0)^2 \right] \qquad (9)$$

yields

$$\tilde{r}_\theta(t) = \frac{A}{2} \mathrm{Re}\left\{ \int_{-L}^{L} p_\theta(u) \left[\exp\left\{ j\left[\omega_0\left(2t - \frac{2u}{c} - 2\tau_0 \right) \right.\right.\right.\right.$$
$$\left.\left.\left. + \alpha\left((t - \tau_0)^2 + \left(t - \tau_0 - \frac{2u}{c} \right)^2 \right) \right] \right\} \right.$$
$$\left. + \exp\left\{ j\left[\frac{4\alpha u^2}{c^2} - \frac{2u}{c}(\omega_0 + 2\alpha(t - \tau_0)) \right] \right\} \right] du \right\}.$$

The first term is centered on the RF carrier frequency ω_0, whereas the second term is not, so low-pass filtering $\tilde{r}_\theta(t)$ gives

$$\hat{r}_\theta(t) = \frac{A}{2} \mathrm{Re}\left\{ \int_{-L}^{L} p_\theta(u) \right.$$
$$\left. \cdot \exp\left\{ j\left[\frac{4\alpha u^2}{c^2} - \frac{2u}{c}(\omega_0 + 2\alpha(t - \tau_0)) \right] \right\} du \right\}.$$

Similarly, it can be shown that mixing $r_\theta(t)$ with

$$\sin\left[\omega_0(t - \tau_0) + \alpha(t - \tau_0)^2 \right]$$

and low-pass filtering gives the quadrature component

$$\tilde{r}_\theta(t) = \frac{A}{2} \mathrm{Im}\left\{ \int_{-L}^{L} p_\theta(u) \right.$$
$$\left. \cdot \exp\left\{ j\left[\frac{4\alpha u^2}{c^2} - \frac{2u}{c}(\omega_0 + 2\alpha(t - \tau_0)) \right] \right\} du \right\}.$$

The real signals $\hat{r}_\theta(t)$ and $\tilde{r}_\theta(t)$, therefore, determine the real and imaginary components of the complex signal

$$C_\theta(t) = \frac{A}{2} \int_{-L}^{L} p_\theta(u) \exp\left\{ j\frac{4\alpha u^2}{c^2} \right\}$$
$$\cdot \exp\left\{ -j\frac{2}{c}(\omega_0 + 2\alpha(t - \tau_0)) u \right\} du. \qquad (10)$$

The effect of the quadratic phase term in (10) will be considered later; for now let us assume that this factor can be removed to obtain

$$\bar{C}_\theta(t) = \frac{A}{2} \int_{-L}^{L} p_\theta(u) \exp\left\{ -j\frac{2}{c}[\omega_0 + 2\alpha(t - \tau_0)] u \right\} du.$$

This last expression can be identified as the Fourier transform of the projection $p_\theta(u)$, that is,

$$\bar{C}_\theta(t) = \frac{A}{2} P_\theta\left[\frac{2}{c}(\omega_0 + 2\alpha(t - \tau_0)) \right]. \qquad (11)$$

The net result is that, at least within the time interval considered, the processed return signal $\bar{C}_\theta(t)$ is the Fourier transform of a projection.

According to the projection-slice theorem, $\bar{C}_\theta(t)$ is a slice at angle θ of the 2-D transform G of the unknown reflectivity density. From (8), the processed return $\bar{C}_\theta(t)$ is available for

$$-\frac{T}{2} + \frac{2(R + L)}{c} \leqslant t \leqslant \frac{T}{2} + \frac{2(R - L)}{c}.$$

So, from (11), $P_\theta(X)$ is determined for $X_1 \leqslant X \leqslant X_2$ with

$$X_1 = \frac{2}{c}\left(\omega_0 - \alpha T + \frac{4\alpha L}{c} \right)$$

$$X_2 = \frac{2}{c}\left(\omega_0 + \alpha T - \frac{4\alpha L}{c} \right). \qquad (12)$$

Thus only the segment of width $X_2 - X_1$ of each slice of G is actually determined. Processing returns from angles satisfying $|\theta| \leqslant \theta_M$ provides samples of $G(X, Y)$ on the polar grid in the annulus segment shown in Fig. 6. Transform points at angle θ are determined from the radar return collected at angle θ. The inner and outer radii, X_1 and X_2, are proportional to the lowest and highest frequencies in the transmitted chirp pulse [7]. This observation follows easily since for a typical SAR, $\omega_0 \pm \alpha T \gg 4\alpha L/c$, so that (12) reduces to

$$X_1 = \frac{2}{c}(\omega_0 - \alpha T)$$

$$X_2 = \frac{2}{c}(\omega_0 + \alpha T). \qquad (13)$$

---

[3] The assumption of superposition is properly questioned. The extent of its validity is carefully discussed by Rihaczek [25].

[4] For t not satisfying (8), the argument of $s(\cdot)$ in (6) can lie outside $\pm T/2$ so that $r_\theta(t)$ will not be correctly given by (7). It is possible, however, to process $r_\theta(t)$ over the slightly larger interval $-(T/2) + (2R/c) \leqslant t \leqslant (T/2) + (2R/c)$ to obtain somewhat improved resolution.
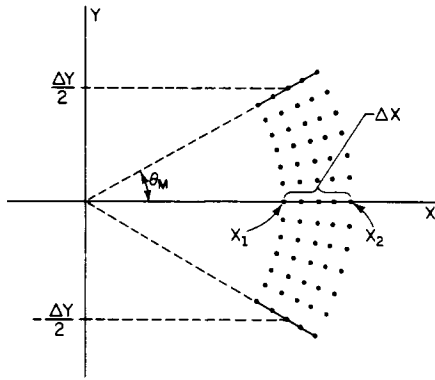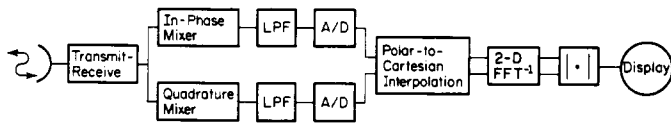
Fig. 6. Annulus segment containing known samples of $G(X, Y)$.

Fig. 7. Required processing for spotlight-mode SAR.

From (4), the lowest and highest frequencies in the transmitted chirp pulse are $\omega_0 - \alpha T$ and $\omega_0 + \alpha T$ which are proportional to X_1 and X_2 in (13).

As remarked earlier, there is no known fast FFT-type algorithm for computing approximate samples of g from polar samples of G. In the case of SAR, an approximation to g is obtained by interpolating the known samples of G to a Cartesian grid, assuming unknown samples (those outside the annulus segment in Fig. 6) to be zero. This may be accomplished in a number of ways [11], e.g., by first linearly interpolating the samples of G on each radial line in Fig. 6 to a set of uniformly spaced vertical lines (resulting in a "keystone" grid [26]). These data are then linearly interpolated in the vertical dimension giving approximate samples of G on a Cartesian grid. After interpolation, an inverse 2-D FFT is employed and the amplitude of g is displayed for viewing [9], [26]. Before FFT processing, the samples of G are windowed to reduce sidelobe levels and are translated to the origin to save computation. The translation has no effect on the amplitude of the FFT output. The required processing for SAR is similar to that for tomography and is summarized in Fig. 7.

C. SAR as a Narrow-Band Version of CAT

The mathematical models for SAR and CAT bear enough resemblance to each other to allow both systems to be explained in terms of the projection-slice theorem. There are important differences, however. In SAR, the line integral involved in the projection is taken perpendicular to the direction in which the radio waves travel. This is in contrast to tomography, where the line integral is taken along the path of the X-rays. Also, a SAR system, utilizing a chirp waveform, determines the transform of the projection rather than the projection itself. Although it is not difficult to convert back and forth between the projection and its transform, this factor may partially explain why spatial domain reconstruction algorithms have not been considered for SAR.

The most striking difference between SAR and tomographic imaging is that SAR data are necessarily narrow-band. As we have seen, the transform domain data in a SAR system are restricted to lie in a small annulus segment with inner and outer edges that are determined by the frequency content of the transmitted chirp. Indeed, if the transmitted waveform is a sinusoid

(zero bandwidth) rather than a chirp, data are obtained at only a single ring in the transform domain [16]. However, if waveforms such as pseudo-random signals or even very short pulses are transmitted, the frequency content of the data in the transform domain is significant. (In fact, according to the model presented, if the SAR *could* transmit an impulse, $s(t) = \delta(t)$, with infinite bandwidth, the SAR imaging equation (6) would provide the projection $p_\theta(u)$ directly, as in tomography.) In general, the range information measured by a coherent SAR may be thought of as consisting of two parts: coarse range information providing the range resolution of the SAR, and fine range information (fractional wavelength range) that makes it possible to obtain high azimuth resolution through coherent processing.

Considering the narrow-band feature of SAR, it may seem surprising that acceptable imagery can be obtained. For example, an edge oriented at an angle $\theta_0 + 90°$ in the ground patch with real reflectivity will have significant frequency content in the transform domain along a line at an angle θ_0. If θ_0 does not fall within the look angle of the radar, such an edge will be obscured. Yet, unlike the attenuation coefficient in CAT, the reflectivity density in SAR is complex. Although the *magnitude* of the observed reflectivity density of resolution cells in the final processed image will not have significant frequency content within the annulus segment in Fig. 6, a random complex reflectivity can be attributed to an assumed distribution of point scatterers (each having random phase) in each resolution cell, giving rise to frequency components over much of the transform plane. Thus a segment of the transform plane displaced from the origin can contain significant information about the magnitude of the overall reflectivity density. This property is similar to holography, where a piece of a hologram contains the information essential for reconstructing a recognizable image. Indeed, a strong connection between SAR and holography has been established [27], [28].

Although SAR systems can produce high-quality imagery, various aberrations, such as coherent speckle, may be observed due to the narrow-band feature. For example, if the target is illuminated with a sinusoid of wavelength λ, then two point reflectors with approximately in-phase reflectivity and displaced in range by an odd multiple of $\lambda/4$ will result in destructive interference.[5] For the case of a transmitted chirp, interference can still occur. Here the response of the SAR system to a point reflector will be approximately a modulated 2-D sinc pulse having the width of a resolution cell (assuming an approximately rectangular region in Fig. 6); responses from adjacent point reflectors in the same resolution cell will thus overlap and interfere either constructively or destructively (see Fig. 8). At the expense of resolution, coherent speckle may be reduced by dividing the Fourier space into several sections and incoherently summing the magnitudes of the responses from each section.

Because SAR is essentially a narrow-band version of CAT, reconstruction algorithms used in one system may be used with only slight modification in the other. In the next section, a modification of the tomographic convolution-backprojection algorithm is introduced for use in SAR. This algorithm permits computation to proceed in step with data collection, since the final integration is performed over θ.

D. Reconstruction via the Backprojection Algorithm

The reconstruction of an image via convolution backprojection is accomplished on the basis of writing the Fourier integral (1) in polar form

---

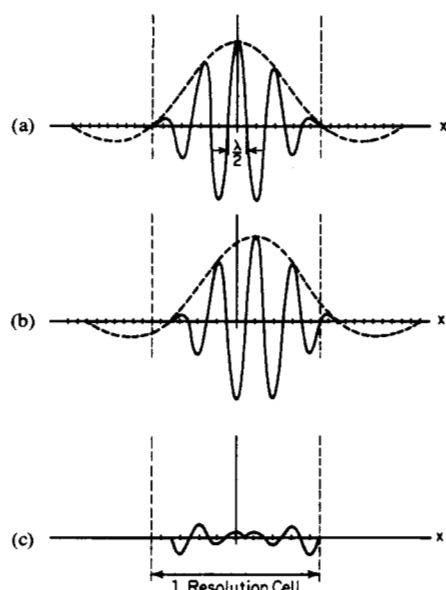[5] This factor is $\lambda/4$ rather than $\lambda/2$ due to two-way travel.

Fig. 8. One-dimensional example of destructive interference. (a) Real part of response from point target at $x = 0$. (b) Real part of response from point target at $x = \lambda/4$. (c) Sum of the responses. (Imaginary parts also destructively interfere.)

$$g(\rho \cos \phi, \rho \sin \phi) = \frac{1}{4\pi^2} \int_{-\pi/2}^{\pi/2} \int_{-\infty}^{\infty} G(r \cos \theta, r \sin \theta)|r|$$
$$\cdot \exp[jr\rho \cos(\phi - \theta)] \, dr \, d\theta$$
$$= \frac{1}{4\pi^2} \int_{-\pi/2}^{\pi/2} \int_{-\infty}^{\infty} P_\theta(r)|r|$$
$$\cdot \exp[jr\rho \cos(\phi - \theta)] \, dr \, d\theta \quad (14)$$

where the second equality follows by the projection-slice theorem (3). The integral over r may be identified as an inverse Fourier transform with argument $\rho \cos(\phi - \theta)$, allowing (14) to be rewritten

$$g(\rho \cos \phi, \rho \sin \phi) = \frac{1}{2\pi} \int_{-\pi/2}^{\pi/2} [p_\theta * k](\rho \cos(\phi - \theta)) \, d\theta$$
$$(15)$$

where

$$k = \mathscr{F}^{-1}[|r|].$$

The tomographic reconstruction algorithm evaluates the convolutions (possibly in the Fourier domain) for each θ, and then approximates the integral as a sum of these results.

In the case of SAR, we have available $P_\theta(r)$, the Fourier transform of the projection, so let us consider using (14) rather than (15). Notice that (14) requires $P_\theta(r)$ for all r, but from (12), the SAR system determines $P_\theta(r)$ over only a relatively small interval centered at $r = 2\omega_0/c$. Therefore, a window function vanishing outside this interval is applied before inverting $P_\theta(r)$ via an inverse FFT. Furthermore, since the known segment of P_θ is offset from the origin, P_θ is translated to the origin and the FFT result compensated accordingly. This is based on rewriting (14) as

$$g(\rho \cos \phi, \rho \sin \phi)$$
$$= \frac{1}{4\pi^2} \int_{-\pi/2}^{\pi/2} \left[\int_0^{X_2 - X_1} P_\theta(r + X_1)|r + X_1|W(r) \right.$$
$$\left. \cdot \exp[jr\rho \cos(\phi - \theta)] \, dr \right] \cdot \exp[jX_1\rho \cos(\phi - \theta)] \, d\theta \quad (16)$$

where X_1 and X_2 are given by (12) and W is a window function which tapers to zero on the interval $[0, X_2 - X_1]$. Finally, note that (16) requires that the inverse transform be evaluated at $\rho \cos(\phi - \theta)$ for various ρ, ϕ, and θ. Therefore, some interpolation of the FFT results is required before summing over θ. In addition, P_θ is available in a SAR system for only a restricted set of look angles as illustrated in Fig. 6. Thus it is desirable to apply a second window before integration over θ.

We have simulated the modified convolution–backprojection algorithm and compared it with the direct Fourier domain algorithm using linear interpolation in each dimension. Initial results show that the backprojection algorithm produces images of somewhat better quality—we hope to make this the subject of a future paper.

IV. ADDITIONAL CONSIDERATIONS IN SAR

A. Resolution and Required Sampling Rate

A SAR system provides transform domain data in the small polar region of the X–Y plane shown in Fig. 6. A definition of resolution in the image (spatial) domain can be motivated by considering the polar region to be approximated by a rectangle of width ΔX and height ΔY (see Fig. 6). The transform of a point reflector at (x_0, y_0) with reflectivity γ is

$$G(X, Y) = \int_{-\infty}^{\infty} \int_{-\infty}^{\infty} \gamma \delta(x - x_0, y - y_0) \cdot$$
$$\cdot \exp[-j(xX + yY)] \, dx \, dy$$
$$= \gamma \exp[-j(x_0 X + y_0 Y)]$$

so that the SAR system response to such a reflector is approximately

$$|\hat{g}(x, y)| = \frac{|\gamma|}{4\pi^2} \left| \int_{X_1}^{X_1 + \Delta X} \int_{-\Delta Y/2}^{\Delta Y/2} \right.$$
$$\cdot \exp[-j(x_0 X + y_0 Y)][\exp j(xX + yY)] \, dY \, dX \Big|$$
$$= \frac{|\gamma|}{4\pi^2} \left| \Delta X \operatorname{sinc}\left(\frac{1}{2}\Delta X(x - x_0)\right) \Delta Y \right.$$
$$\left. \cdot \operatorname{sinc}\left(\frac{1}{2}\Delta Y(y - y_0)\right) \right|.$$

The first zero crossings in the response occur at $x - x_0 = 2\pi/\Delta X$ and $y - y_0 = 2\pi/\Delta Y$. Therefore, as a rough guide, resolution of two point reflectors having equal reflectivity requires that the reflectors be separated by more than $2\pi/\Delta X$ in the x dimension and $2\pi/\Delta Y$ in the y dimension. From (13) and Fig. 6 we have, for $\theta_M \ll 1$, that $\Delta X \approx 4\alpha T/c$ and $\Delta Y \approx 2[(2\omega_0/c)\sin\theta_M]$. Thus the system resolution is defined as[6]

$$\delta_x = \frac{2\pi}{\Delta X} \approx \frac{\pi c}{2\alpha T} \quad (17)$$

$$\delta_y = \frac{2\pi}{\Delta Y} \approx \frac{\pi c}{2\omega_0 \sin\theta_M}. \quad (18)$$

It is common in the SAR literature to refer to an area of size δ_x by δ_y in the reconstructed image as a *resolution cell*. Notice that the range resolution depends on only the bandwidth of the

---

[6]Although (17) and (18) are useful in practice, it requires more than a single pair of numbers (δ_x, δ_y) to precisely characterize resolution, because an actual target is composed of many interfering reflectors of varying intensities. See [25], [29] for further discussion.
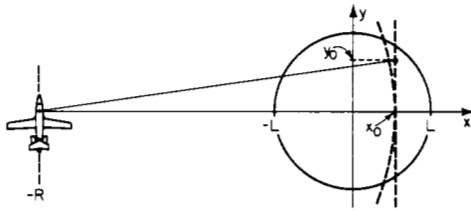
Fig. 9. Wavefront curvature over the target field.

transmitted signal, whereas the azimuth resolution depends on the center frequency and also on the range of look angles. Therefore, the resolving phenomena are entirely different in range and azimuth. Also, the necessary range of look angles to provide $\delta_y = \delta_x$ is actually quite small. For a typical SAR, ω_0 may be twenty times αT, giving $2\theta_M \approx 6°$.

Let us next consider an appropriate sampling rate for the transform in the polar region of Fig. 6. The usual sampling theorem will apply only if the inverse transform of the known segment of $G(X, Y)$ is spatially limited. Of course, this cannot be, since a signal cannot be both frequency limited and spatially limited. However, it is known that the true $g(x, y)$ is spatially limited by the radar antenna beam to a region of half-width L. Therefore, sampling rates in the X and Y directions should be *at least*

$$f_s = \frac{1}{2\pi}(2L) \text{ samples/rad.}$$

This corresponds to an image raster having

$$\left(\frac{L}{\pi} \cdot \Delta X = \frac{2L}{\delta_x}\right) \times \left(\frac{L}{\pi} \cdot \Delta Y = \frac{2L}{\delta_y}\right) = 4L^2/\delta_x\delta_y$$

samples or resolution cells in all. In practice, sampling rates somewhat higher than f_s are used.

B. Curvature of the Wavefront

As we have previously noted, SAR projections are not really taken over straight lines, but are taken over slight curves due to the outward propagation of waves from the transmitter. Two conditions must simultaneously be satisfied in order that this effect be neglected. First, the range error due to wavefront curvature over the target field must be less than a resolution cell, i.e.,
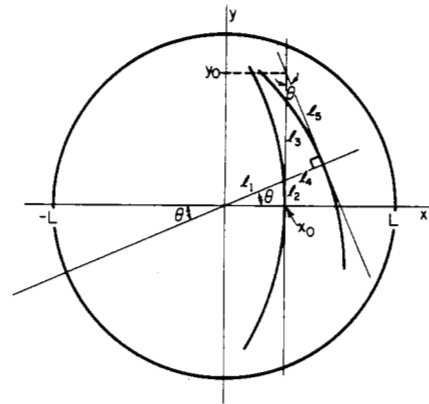
$$\frac{L^2}{2R} < \delta_x. \tag{19}$$

Condition (19) is obtained with the help of Fig. 9. The range error at a point (x_0, y_0) is

$$\left[(R + x_0)^2 + y_0^2\right]^{1/2} - (R + x_0)$$

$$= (R + x_0)\left\{\left[1 + \frac{y_0^2}{(R + x_0)^2}\right]^{1/2} - 1\right\}$$

$$\approx (R + x_0)\left\{1 + \frac{y_0^2}{2(R + x_0)^2} - 1\right\} \tag{20}$$

$$\approx \frac{y_0^2}{2R} \tag{21}$$

where the approximations hold since $R \gg x_0, y_0$. Evaluating (21) at the largest value of y_0 within the target patch gives (19).

A second condition arises since a SAR system coherently

Fig. 10. Wavefront curvature for projection angles 0 and θ.

combines projections from many different angles. To preserve coherence, the range error due to wavefront curvature at a particular point must vary by no more than a small fraction of a wavelength through the full range of look angles. To analyze this effect, consider Fig. 10 which shows the wavefront curvature at the point (x_0, y_0) due to look angles 0 and θ. Evaluating the l_i gives

$$l_1 = \frac{x_0}{\cos\theta}$$

$$l_2 = l_1 \sin\theta = x_0 \tan\theta$$

$$l_3 = y_0 - l_2 = y_0 - x_0 \tan\theta$$

$$l_4 = l_3 \sin\theta = y_0 \sin\theta - x_0 \frac{\sin^2\theta}{\cos\theta}$$

$$l_5 = l_3 \cos\theta = y_0 \cos\theta - x_0 \sin\theta.$$

The range error at point (x_0, y_0) for a projection at angle θ is

$$\left[(R + l_1 + l_4)^2 + l_5^2\right]^{1/2} - (R + l_1 + l_4) \approx \frac{l_5^2}{2(R + l_1 + l_4)} \tag{22}$$

similar to (20). For a typical SAR system $R \gg l_1 + l_4$, so, from (21) and (22), the difference in wavefront curvature from a projection at angle 0 and a projection at angle θ is approximately

$$D = \frac{1}{2R}\left(y_0^2 - l_5^2\right)$$

$$= \frac{1}{2R}\left(y_0^2 \sin^2\theta + 2x_0 y_0 \sin\theta \cos\theta - x_0^2 \sin^2\theta\right). \tag{23}$$

Given the constraints $\theta \leq \theta_M$ and $x_0^2 + y_0^2 \leq L^2$, numerical optimization could be applied to (23) to obtain the maximum deviation. Instead, however, let us examine two special cases which would appear to yield large deviations:

$$1) \quad x_0 = 0, \quad y_0 = L$$

$$2) \quad x_0 = y_0 = \frac{L}{\sqrt{2}}.$$

For case 1), the deviation (23) reduces to

$$D_1 = \frac{L^2 \sin^2\theta}{2R} \leq D_1^{\max} \triangleq \frac{L^2 \sin^2\theta_M}{2R}.$$

For case 2) we obtain

$$D_2 = \frac{L^2 \sin\theta \cos\theta}{2R} = \frac{L^2 \sin 2\theta}{4R} \leq D_2^{\max} \triangleq \frac{L^2 \sin 2\theta_M}{4R}$$

where the inequality assumes $\theta_M \leqslant \pi/4$. For θ_M in this range, we have $D_2^{max} \geqslant D_1^{max}$. Hence, to preserve coherency we require that D_2^{max} be much smaller than a fraction of a wavelength, i.e.,

$$\frac{L^2 \sin 2\theta_M}{4R} \ll \frac{c}{8\omega_0} = \frac{\lambda}{8}. \qquad (24)$$

Assuming $\delta_x = \delta_y$ in (17) and (18), condition (24) will be more severe than condition (19). If the target region to be mapped is too large to satisfy (24), the area may be mapped in smaller segments, using either antenna steering of a phased array or digital presumming methods [30]. Alternatively, the backprojection method may be applied even in the case of projections over curves in a manner described in [31].

C. Quadratic Phase Term

It was assumed earlier that the quadratic phase term in (10) can be removed. This can be partially accomplished by inverse transforming $C_\theta(t)$, multiplying by $\exp\{-j(4\alpha u^2/c^2)\}$, and then retransforming. However, there is some error in this procedure since $C_\theta(t)$ is not known for all t. If the step to remove the quadratic phase factor is omitted, the image suffers a consequent loss of resolution. However, if the inequality

$$\frac{4\alpha L^2}{c^2} \ll \frac{\pi}{2} \qquad (25)$$

is satisfied, then the loss of resolution will be small. We previously saw that the number of resolution cells in the reconstructed image will be

$$N^2 = \frac{4L^2}{\delta_x \delta_y}$$

where δ_x and δ_y are given by (17) and (18). Assuming $\delta_y \approx \delta_x$ and substituting from (17) gives

$$N^2 = \frac{16L^2\alpha^2T^2}{\pi^2c^2}. \qquad (26)$$

Defining the time–bandwidth product (TBW) of the transmitted chirp as

$$\text{TBW} = T \cdot \frac{2\alpha T}{2\pi} = \frac{\alpha T^2}{\pi}$$

and using (26), condition (25) becomes

$$N^2 \ll 2\,\text{TBW}. \qquad (27)$$

Condition (27) implies that the quadratic phase term can be neglected as long as the TBW is sufficiently large compared with N^2.

These relations show that neglecting the quadratic phase term imposes a limit on the resolution using SAR processing with chirp waveforms. Compensating for this term, as suggested above, is necessary for improved resolution.

D. Effect of Doppler and Time-Varying Range

Thus far, little mention has been made of the fact that the radar unit is moving as measurements are made—the radar unit was simply assumed to be placed at discrete positions along the flight path as projection data were gathered. Due to the motion of the aircraft, there is a Doppler effect which must be considered.

From Fig. 5 there is a radial component of the aircraft velocity $v_r = v \sin\theta$, where v is the speed of the aircraft. Therefore, the received signal, $r_\theta(t)$ in (6), is more accurately given by
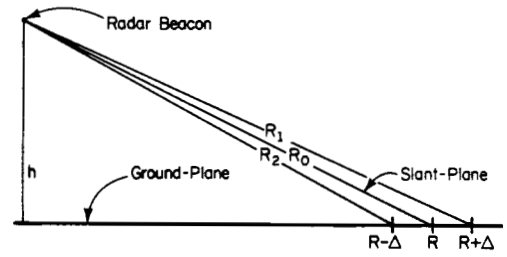

Fig. 11. Side view of radar flown at height h.

$$r_\theta(t) = A \cdot \text{Re}\left\{ \int_{-L}^{L} p_\theta(u) s\left(at - \frac{2(R+u)}{c}\right) du \right\} \qquad (28)$$

with

$$a = \left(1 + \frac{v_r}{c}\right)^2 \approx 1 + \frac{2v_r}{c}$$

where the square is due to two-way travel. Instead of (9), the reference used for demodulation should then be

$$\cos\left[\omega_0(at - \tau_0) + \alpha(at - \tau_0)^2\right]. \qquad (29)$$

Equations (28) and (29) give the correction for a target point at the center of the ground patch. The Doppler shift will vary slightly from point to point within the target patch since the angle from the radar and, therefore, the radial component of the aircraft velocity will vary slightly from the center to either side of the patch. Thus the reference waveform given by (29) cannot completely compensate for the Doppler effect. Assuming $\theta = 0$ in Fig. 5, and considering an extreme case, the radial component of the aircraft velocity for a point p^* at the top of the target patch at a distance R from the radar is approximately

$$v_r^* = v \sin\left(\tan^{-1}\frac{L}{R}\right) \approx v\frac{L}{R}.$$

The difference between the round-trip propagation times to the center of the target patch and to p^* is

$$\frac{2R}{c} - \frac{2R}{c + v_R^*} = \frac{2R}{c}\left(1 - \frac{1}{1 + \frac{vL}{cR}}\right) \approx \frac{2vL}{c^2}. \qquad (30)$$

To preserve the ability to measure fractional wavelengths (needed for high azimuth resolution), we require that c times (30) be less than one-quarter wavelength, i.e.,

$$\frac{2vL}{c} < \frac{\lambda_0}{4} \quad \text{or} \quad \frac{v}{c} < \frac{\lambda_0}{8L}$$

where $\lambda_0 = 2\pi c/\omega_0$. Thus for a given aircraft velocity, the variation in Doppler shift limits the target size. Notice that this condition is considerably different from the limitation (24) imposed by wavefront curvature.

Another factor that requires compensation is time-varying range. If the aircraft in Fig. 5 flies a straight path, the range to the center of the target patch will vary considerably. Thus R in (28) is actually a function of θ, and the demodulating waveform, (29), must be modified accordingly. Alternatively, a fixed high-frequency demodulator can be used, followed by a time-varying low-frequency demodulator that compensates for both time-varying range and Doppler. The second demodulator can be implemented digitally.

E. Modification of Results for Slant-Plane Geometry

In the previous analyses we have neglected the fact that the radar operates in the slant plane at some nonzero height h above

the ground plane, as shown in Fig. 11. Therefore, it is necessary to modify our results by stretching the range dimension. The amount of compensation required is easily found by considering two point targets in the ground patch at distance R_1 and R_2 from the radar, as shown in Fig. 11. Let the locations in the ground plane be $R + \Delta$ and $R - \Delta$. The targets are, therefore, separated by a true distance of 2Δ. From the radar's point of view, however, the separation is

$$R_1 - R_2 = \sqrt{h^2 + (R + \Delta)^2} - \sqrt{h^2 + (R - \Delta)^2}$$
$$\approx \sqrt{h^2 + R^2 + 2R\Delta} - \sqrt{h^2 + R^2 - 2R\Delta}$$

for $R \gg \Delta$. This can be further approximated as

$$R_1 - R_2 = R_0 \left[\sqrt{1 + \frac{2R\Delta}{R_0^2}} - \sqrt{1 - \frac{2R\Delta}{R_0^2}} \right]$$
$$\approx R_0 \left[1 + \frac{R\Delta}{R_0^2} - \left(1 - \frac{R\Delta}{R_0^2} \right) \right]$$
$$= 2\Delta \frac{R}{R_0}.$$

Therefore, to obtain the true separation, 2Δ, it is necessary to stretch the range dimension by R_0/R. Taking this into account, the derivation in Section III can be easily modified, beginning with

$$r_\theta(t) = A \cdot \text{Re} \left\{ \int_{-L}^{L} p_\theta(u) s \left(t - \frac{2\left(R_0 + u\frac{R}{R_0} \right)}{c} \right) du \right\}$$

as a replacement for (6), where p_θ is the projection of the reflectivity density in the ground plane, R is the distance from the projection of the radar onto the ground plane to the center of the target patch, and R_0 is the true distance (in the slant plane) from the radar to the center of the target patch. Note that R/R_0 will vary as a function of range, and therefore as a function of θ for a straight-line flight path. Thus the modification required for each projection will, in general, be different.

V. CONCLUSION

A tomographic formulation of spotlight-mode SAR has been presented. We have shown that a chirped SAR operating in spotlight mode records a portion of the Fourier transform of a central projection of the ground patch at each look angle. This establishes that "polar format Doppler processing," used in SAR, is a form of tomographic reconstruction that may be conveniently described by the projection-slice theorem. The tomographic interpretation permits, we believe, a conceptually simpler understanding of SAR than an analysis based solely on Doppler concepts. An important benefit in making the connection between SAR and CAT is that algorithms and signal processing methods developed in one field may be applied to the other. For example, it was shown how the convolution-backprojection algorithm, that is widely used in commercial CAT scanners, can be modified for use in SAR.

Various issues concerning speckle, resolution, wavefront curvature, residual quadratic phase errors, and the effects of Doppler and time-varying range have been considered. In particular, it was shown that the terrain patch size is limited by the effects of wavefront curvature and Doppler.

REFERENCES

[1] H. J. Scudder, "Introduction to computer aided tomography," *Proc. IEEE*, vol. 66, pp. 628–637, June 1978.
[2] G. T. Herman, Ed., *Image Reconstruction from Projections*. New York: Springer, 1979.
[3] C. W. Sherwin, J. P. Ruina, and R. D. Rawcliffe, "Some early developments in synthetic aperture radar systems," *IRE Trans. Mil. Electron.*, vol. MIL-6, pp. 111–115, Apr. 1962.
[4] W. M. Brown and C. J. Palermo, "Theory of coherent systems," *IRE Trans. Mil. Electron.*, vol. MIL-6, pp. 187–196, Apr. 1962.
[5] W. M. Brown and L. J. Porcello, "An introduction to synthetic aperture radar," *IEEE Spectrum*, vol. 6, pp. 52–62, Sept. 1969.
[6] K. Tomiyasu, "Tutorial review of synthetic-aperture radar (SAR) with applications to imaging of the ocean surface," *Proc. IEEE*, vol. 66, pp. 563–583, May 1978.
[7] J. L. Walker, "Range-Doppler imaging of rotating objects," *IEEE Trans. Aerosp. Electron. Syst.*, vol. AES-16, pp. 23–52, Jan. 1980.
[8] W. M. Brown and R. J. Fredricks, "Range-Doppler imaging with motion through resolution cells," *IEEE Trans. Aerosp. Electron. Syst.*, vol. AES-5, pp. 98–102, Jan. 1969.
[9] "Advanced synthetic array radar techniques," First Interim Report, Radar and Optics Division, Environmental Research Institute of Michigan, unclassified excerpts, Mar. 1976, available from DTIC as Tech. Rep. AFAL-TR-75-87.
[10] R. M. Mersereau, "Recovering multidimensional signals from their projections," *Comput. Graph. Image Proc.*, vol. 1, pp. 179–195, Oct. 1973.
[11] R. M. Mersereau and A. V. Oppenheim, "Digital reconstruction of multidimensional signals from their projections," *Proc. IEEE*, vol. 62, pp. 1319–1338, Oct. 1974.
[12] M. I. Skolnik, *Introduction to Radar Systems*. 2nd ed. New York: McGraw-Hill, 1980, pp. 34–44.
[13] G. Wade, S. Elliott, I. Khogeer, G. Flesher, J. Eisler, D. Mensa, N. Ramesh, and G. Heidbreder, "Acoustic echo computer tomography," in *Acoustic Holography*, vol. 8, A. Metherell, ed. New York: Plenum, 1978.
[14] D. Mensa, G. Heidbreder, and G. Wade, "Aperture synthesis by object rotation in coherent imaging," *IEEE Trans. Nucl. Sci.*, vol. NS-27, pp. 989–998, Apr. 1980.
[15] D. Mensa and G. Heidbreder, "Bistatic synthetic-aperture radar imaging of rotating objects," *IEEE Trans. Aerosp. Electron. Syst.*, vol. AES-18, pp. 423–431, July 1982.
[16] C. Chen and H. C. Andrews, "Multifrequency imaging of radar turnable data," *IEEE Trans. Aerosp. Electron. Syst.*, vol. AES-16, pp. 15–22, Jan. 1980.
[17] G. T. Herman, *Image reconstruction from Projections*. New York: Academic Press, 1980.
[18] D. L. Mensa, S. Halevy, and G. Wade, "Coherent Doppler tomography for microwave imaging," *Proc. IEEE*, vol. 71, no. 2, pp. 254–261, Feb. 1983.
[19] W. M. Brown, "Walker model for radar sensing of rigid target fields," *IEEE Trans. Aerosp. Electron. Syst.*, vol. AES-16, pp. 104–107, Jan. 1980.
[20] H. H. Stark, J. W. Woods, I. Paul, and R. Hingorani, "Direct Fourier reconstruction in computer tomography," *IEEE Trans. Acoust., Speech, Signal Process.*, vol. ASSP-29, pp. 237–245, Apr. 1981.
[21] A. V. Oppenheim, G. V. Frisk, and D. R. Martinez, "An algorithm for the numerical evaluation of the Hankel transform," *Proc. IEEE*, vol. 66, pp. 264–265, Feb. 1978.
[22] A. J. Jerri, "Towards a discrete Hankel transform and its applications," *J. Appl. Anal.*, vol., 7, pp. 97–109, 1978.
[23] S. M. Candel, "Dual algorithms for fast calculation of the Fourier-Bessel transform," *IEEE Trans. Acoust., Speech, Signal Process.*, vol. ASSP-29, pp. 963–972, Oct. 1981.
[24] D. W. Dearholt and W. R. McSpadden, *Electromagnetic Wave Propagation*. New York: McGraw-Hill, 1973.
[25] A. W. Rihaczek, *Principles of High-Resolution Radar*. New York: McGraw-Hill, 1969, pp. 331–349.
[26] D. A. Schwartz, "Analysis and experimental investigation of three synthetic aperture radar formats," Coordinated Sci. Lab., Univ. of Illinois, Tech. Rep. T-94, Mar. 1980 (M.S. thesis).
[27] E. N. Leith, "Quasi-holographic techniques in the microwave region," *Proc. IEEE*, vol. 59, pp. 1305–1318, Sept. 1971.
[28] W. E. Kock, *Radar, Sonar, and Holography*. New York: Academic Press, 1973.
[29] R. O. Harger, *Synthetic Aperture Radar Systems: Theory and Design*. New York: Academic Press, 1970.
[30] J. C. Kirk, "A discussion of digital processing in synthetic aperture radar," *IEEE Trans. Aerosp. Electron. Syst.*, vol. AES-11, pp. 326–337, May 1975.
[31] B. K. P. Horn, "Density reconstruction using arbitrary ray-sampling schemes," *Proc. IEEE*, vol. 66, pp. 551–562, May 1978.